ACS NANO
www.acsnano.org
ARTICLE

Quasiparticle Scattering in the Rashba Semiconductor BiTeBr: The Roles of Spin and Defect Lattice Site

Christopher John Butler,[†] Po-Ya Yang,[†] Raman Sankar,[‡,§] Yen-Neng Lien,[†] Chun-I Lu,[†] Luo-Yueh Chang,[⊥] Chia-Hao Chen,[⊥] Ching-Ming Wei,[∥] Fang-Cheng Chou,[§,⊥,¶] and Minn-Tsong Lin[*,†,∥,#]

[†]Department of Physics and [§]Center for Condensed Matter Sciences, National Taiwan University, Taipei 10617, Taiwan
[⊥]National Synchrotron Radiation Research Center, Hsinchu 30076, Taiwan
[‡]Institute of Physics, [∥]Institute of Atomic and Molecular Sciences, and [#]Research Center for Applied Sciences, Academia Sinica, Taipei 11529, Taiwan
[¶]Taiwan Consortium of Emergent Crystalline Materials (TCECM), National Science Council, Taipei 10622, Taiwan

Supporting Information

ABSTRACT: **Observations of quasiparticle interference have been used in recent years to examine exotic carrier behavior at the surfaces of emergent materials, connecting carrier dispersion and scattering dynamics to real-space features with atomic resolution. We observe quasiparticle interference in the strongly Rashba split 2DEG-like surface band found at the tellurium termination of BiTeBr and examine two mechanisms governing quasiparticle scattering: We confirm the suppression of spin-flip scattering by comparing measured quasiparticle interference with a spin-dependent elastic scattering model applied to the calculated spectral function. We also use atomically resolved STM maps to identify point defect lattice sites and spectro-microscopy imaging to discern their varying scattering strengths, which we understand in terms of the calculated orbital characteristics of the surface band. Defects on the Bi sublattice cause the strongest scattering of the predominantly Bi 6p derived surface band, with other defects causing nearly no scattering near the conduction band minimum.**

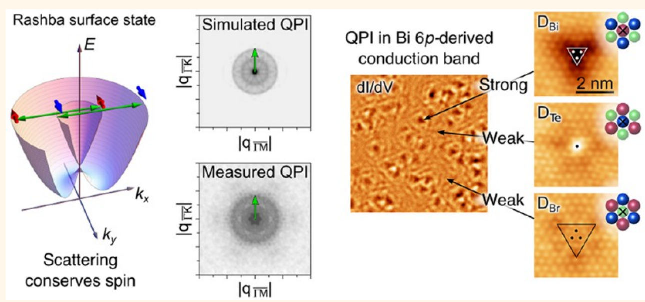

KEYWORDS: *scanning tunneling microscopy, scanning tunneling spectroscopy, polar surfaces, Rashba semiconductor, quasiparticle interference, defect-dependent scattering*

The semiconductor compounds BiTeX (X = Cl, Br, I) combine strong intrinsic spin−orbit coupling with an inversion symmetry breaking layered structure to give rise to a giant Rashba spin splitting. Unlike previous well-known systems hosting strongly Rashba-split surface states, such as the high-Z metal surfaces and surface alloys,[1,2] they have a bulk band gap that gives desirable electrical tunability and greater ease of integration with established device architectures. Although usually topologically trivial, they share functional properties reminiscent of the topological insulators, namely, the combination of a bulk gap with surface Fermi contours of high-mobility 2-D and spin-momentum-locked carriers. These properties were first observed in BiTeI, in which a strong Rashba splitting in both the conduction and valence bands was found to be driven by the combination of an inversion symmetry breaking non-centrosymmetric structure and strong intrinsic spin−orbit interaction,[3] leading to unusual bulk magneto-transport properties.[4−6] The polar structure of BiTeX has been shown to induce strong surface band bending, which shifts either the conduction or valence band to the Fermi level, depending on the polarity of the chosen surface termination.[7,8] This gives rise to either a two-dimensional electron (or hole) gas at the Te termination (or X termination). This combination of the rich physics of two-dimensional systems[9] with gate-tunability and the opportunities arising from a strong Rashba splitting[10] may allow the realization of phenomena such as a universal intrinsic Hall conductivity[11] and various proposed electrically controlled spintronic devices.[10,12−14] Moreover, it has been reported that under some circumstances BiTeX may exhibit a topologically

Received: June 21, 2016
Accepted: September 23, 2016
Published: September 23, 2016

DOI: 10.1021/acsnano.6b04109
ACS Nano 2016, 10, 9361−9369

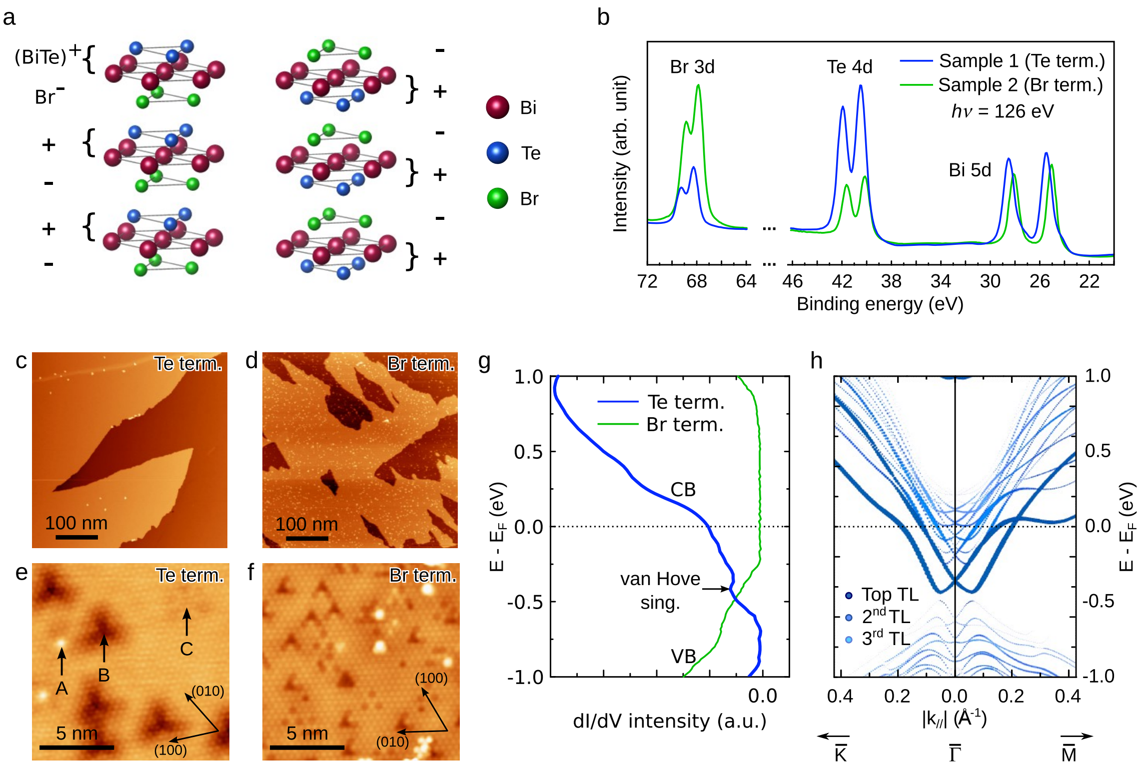

Figure 1. Polar surface terminations of non-centrosymmetric BiTeBr. (a) Depictions of the surface structure for the Te- and Br-terminated surfaces of cleaved BiTeBr. (b) XPS curves for differently terminated samples, showing a polarization-induced binding energy shift between doublets acquired from the respective terminations. (c and d) STM images (both using $V = 2$ V, $I = 0.2$ nA) showing large-scale uniformly terminated surfaces. (e and f) Zoom-in STM images of the Te- and Br-terminated surfaces ($V = 50$ mV, $I = 0.2$ nA and $V = -1.5$, $I = 0.6$ nA, respectively), showing hexagonal surface lattices and characteristic point defects. (g) Tunneling spectroscopy curves taken on each surface, showing electron accumulation at the positively charged Te termination. The small peak at −0.42 eV is attributed to a van Hove singularity at the conduction band minimum, which may arise due to the strong Rashba splitting. (h) Surface-projected band structure calculated for the first three trilayers of the Te termination, showing the strongly Rashba spin split band localized in the surface trilayer (dark blue).

nontrivial phase, giving rise to an inversion asymmetric topological insulator.[15−17]

In contrast with BiTeI and BiTeCl, it has been reported that BiTeBr may lack a non-centrosymmetric structure of the $P3\bar{m}1$ space group, instead having a CdI_2-like structure belonging to the $P3m1$ space group, with mixed, nonpolar terminations and no Rashba effect.[18−20] However, ARPES measurements by Sakano *et al.* indicate that BiTeBr shares the same non-centrosymmetric and polar structure as the other BiTeX compounds.[21] In the ordered phase, BiTeBr is expected to have some advantages over BiTeI and BiTeCl. It has been shown to have a larger Rashba splitting, wider band gap, and better chemical stability as compared with BiTeCl.[20−22] It also has a more isotropic energy dispersion of the surface bands as compared with BiTeI and a larger surface polarization, causing a much larger splitting of the surface bands from the bulk conduction band.[20,21,23] For these reasons it is likely that BiTeBr is the most promising of the BiTeX family for application in spintronic devices.

Scanning tunneling microscopy (STM) observations of quasiparticle interference (QPI) have been used in the past to investigate the role of spin in scattering at strongly spin−orbit-coupled metallic surfaces such as Bi(110),[24] among other systems.[25,26] They have also been used to reveal exotic carrier behaviors at the surfaces of emergent materials including in superconductors and heavy Fermion systems,[27,28] in topological insulators, to discover the suppression of backscattering due to spin-momentum-locking in the topological surface state,[29−31] and most recently in 3-D Dirac and Weyl semimetals.[32,33] Recently, Kohsaka *et al.* used observations of QPI phenomena to confirm the electron-like or hole-like dispersion of carriers at the polar surfaces of BiTeI.[34]

Such observations rely on the presence of defects, usually point defects such as impurities. Distinctions have been made theoretically between magnetic and nonmagnetic impurities in superconductors, due to coherence factors,[35] and in more general systems[36,37] (though it is not anticipated that impurity magnetic moment has any observable effect in normal QPI observations[37,38]). In general, however, point defects of various types have otherwise been treated simply as generic scattering centers without further distinctions being made.

In this work, we take the 2DEG-like surface band at the Te termination of our ordered, non-centrosymmetric BiTeBr crystals as a framework in which to demonstrate and explain two mechanisms governing quasiparticle scattering: (1) the spin-based selection of allowed scattering events due to the Rashba-like spin texture of the surface band and (2) the way in which point defects on different lattice sites couple differently to the surface band due to its orbital characteristics, controlling various defects' scattering strengths. This last point in particular may be generalized to help understand transport properties and scattering in a wide range of existing and emergent systems.

RESULTS

XPS and STM Characterization. X-ray photoelectron spectroscopy (XPS) curves taken on multiple samples show

DOI: 10.1021/acsnano.6b04109
ACS Nano 2016, 10, 9361−9369

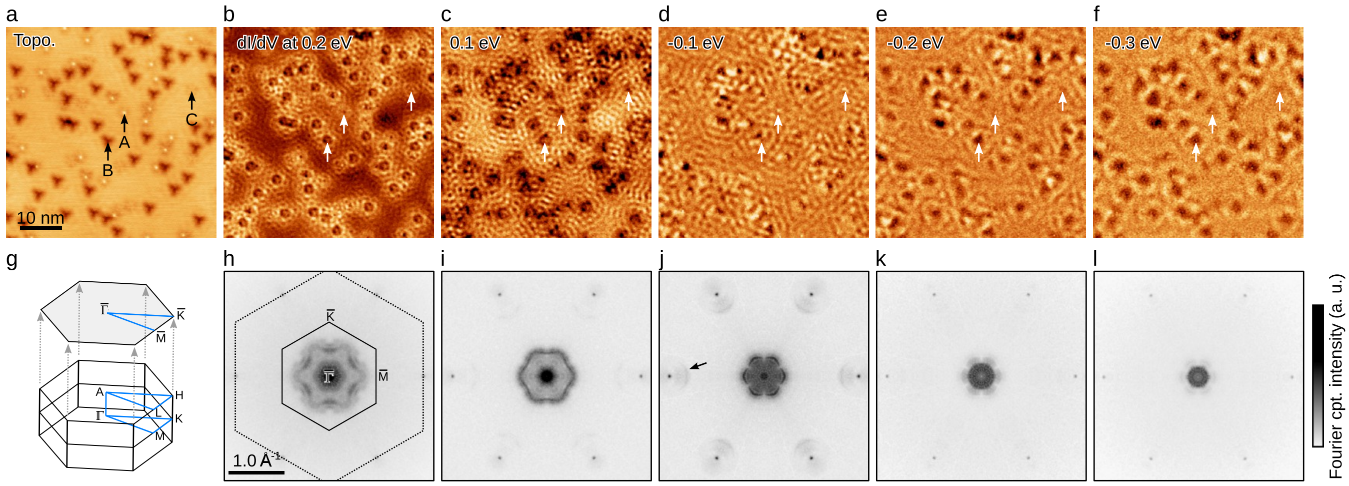

Figure 2. Scattering of electron-like quasiparticles at the Te-terminated surface. (a) STM topography showing three distinct types of point defect (V = 0.1 V, I = 0.3 nA) and (b−f) the corresponding dI/dV maps at various bias voltages, showing quasiparticle standing waves. (g) First BZ and its surface projection, in which the quasiparticle scattering patterns are oriented according to the atomic reciprocal lattice point positions. (h−l) Corresponding symmetrized 2-D FFT images corresponding to the dI/dV maps (b−f), with the surface BZ boundary marked as a solid hexagon. The zone encompassing all allowed scattering vectors is marked with a dotted hexagon. A signature of inter-BZ scattering can be seen at some energies, appearing most prominently in panel (j) and marked with a black arrow.

either of two tendencies, exemplified in the curves for samples 1 and 2 shown in Figure 1b. The relative doublet intensities for each element reveal the relative depth of each layer below the surface, due to the small photoelectron inelastic mean free path (E_{ph} = 126 eV). The inversion of intensity ratio between Te 4d and Br 3d doublets between samples 1 and 2 indicates the inverse stacking orders depicted in Figure 1a. A small relative binding energy shift of around 0.5 eV between the two spectra is attributed to the opposite surface polarizations of the two terminations (see Supporting Information).

Large-scale STM images acquired on Te- and Br-terminated samples, shown in Figure 1c and d, reveal uniformly terminated surfaces unlike those found on BiTeI, which have a domain-like distribution of Te- and I-terminated regions of various scales.[8,34,39,40] For each BiTeBr sample, both XPS and STM measurements indicated the same termination at multiple regions across the cleaved surface, suggesting a high likelihood of single-domain crystals, consistent with observations reported recently by Fiedler *et al.*[41]

Zoom-in STM images on each surface, shown in Figure 1e and f, reveal hexagonal surface lattices with numerous defects. The Br-terminated surface invariably features many highly mobile adatoms and clusters that make prolonged stable STM measurements very difficult, a challenge that has also been reported for the I-terminated surface of BiTeI.[40] Three types of characteristic point defects are found at the Te termination, labeled in Figure 1e as types A (small round protrusions), B (with three dark lobes), and C (very faint, with a dark center surrounded by three dark lobes).

Scanning tunneling spectroscopy (STS) measurements, shown in Figure 1g, reveal the effects of surface polarization induced band bending. Most notably, at the Te termination the conduction band bends below the Fermi energy, creating an electron accumulation layer. A small peak at −0.42 eV may represent a van Hove singularity associated with the minimum of the Rashba split surface band as reported previously for the Te termination of BiTeI.[42] Although this peak appears to be broadened in comparison with van Hove singularities found previously in metal systems,[25,26,43] this may be because the sample lacks the high uniformity of the 3-D Coulomb potential imposed by screening in metal surfaces. For comparison with the STS curve, the planar projected band structures, calculated for each of the top three trilayers (TLs) of the Te termination, are shown in Figure 1h. The band structure was calculated in accordance with DFT as described in the Methods section. The calculated Rashba parameter is α_R = 2.77 eV·Å. This surface band provides the platform from which we investigate the detailed roles of spin and defect chemistry in the scattering of Rashba split 2-D carriers and is the focus for the remainder of this work.

Quasiparticle Interference at the Te-Terminated Surface. Observations of QPI at the Te termination are shown in Figure 2. Maps of dI/dV intensity, acquired in the area shown in the topograph in Figure 2a, are shown in Figure 2b−f. They confirm the expected tendency that with decreasing energy the wavelengths of quasiparticle standing waves increase; that is, the scattering wavevectors between initial and final Bloch states on each constant energy contour (CEC), $\vec{q} = \vec{k}_f - \vec{k}_i$, generally decrease. This can be seen in the dI/dV maps' respective 2-D Fourier transform images, shown in Figure 2h−l. These indicate electron-like quasiparticle dispersion, as has also been observed in QPI at the Te termination of BiTeI by Kohsaka *et al.*[34] Evidence of quasiparticle scattering between the first and extended Brillouin zones (BZs), observed by Kohsaka *et al.*, can also be seen in this work, marked by a black arrow in Figure 2j. On close inspection of real-space dI/dV maps, it can be seen that the most prominent quasiparticle standing waves occur around the dark three-lobed defects labeled as type B in Figure 1e, while standing waves are weak or nonexistent around other defects. We return to this effect below in the discussion of data presented in Figure 5.

We now make a comparison of the dispersive behavior found in measured QPI and that simulated by computing the spin-dependent scattering probability (SSP) using a method somewhat similar to that used by Roushan *et al.* to investigate QPI in $Bi_{1-x}Sb_x$.[29] SSP patterns are computed from the CEC plots. In the work by Roushan *et al.*, these CECs were

DOI: 10.1021/acsnano.6b04109
ACS Nano 2016, 10, 9361−9369

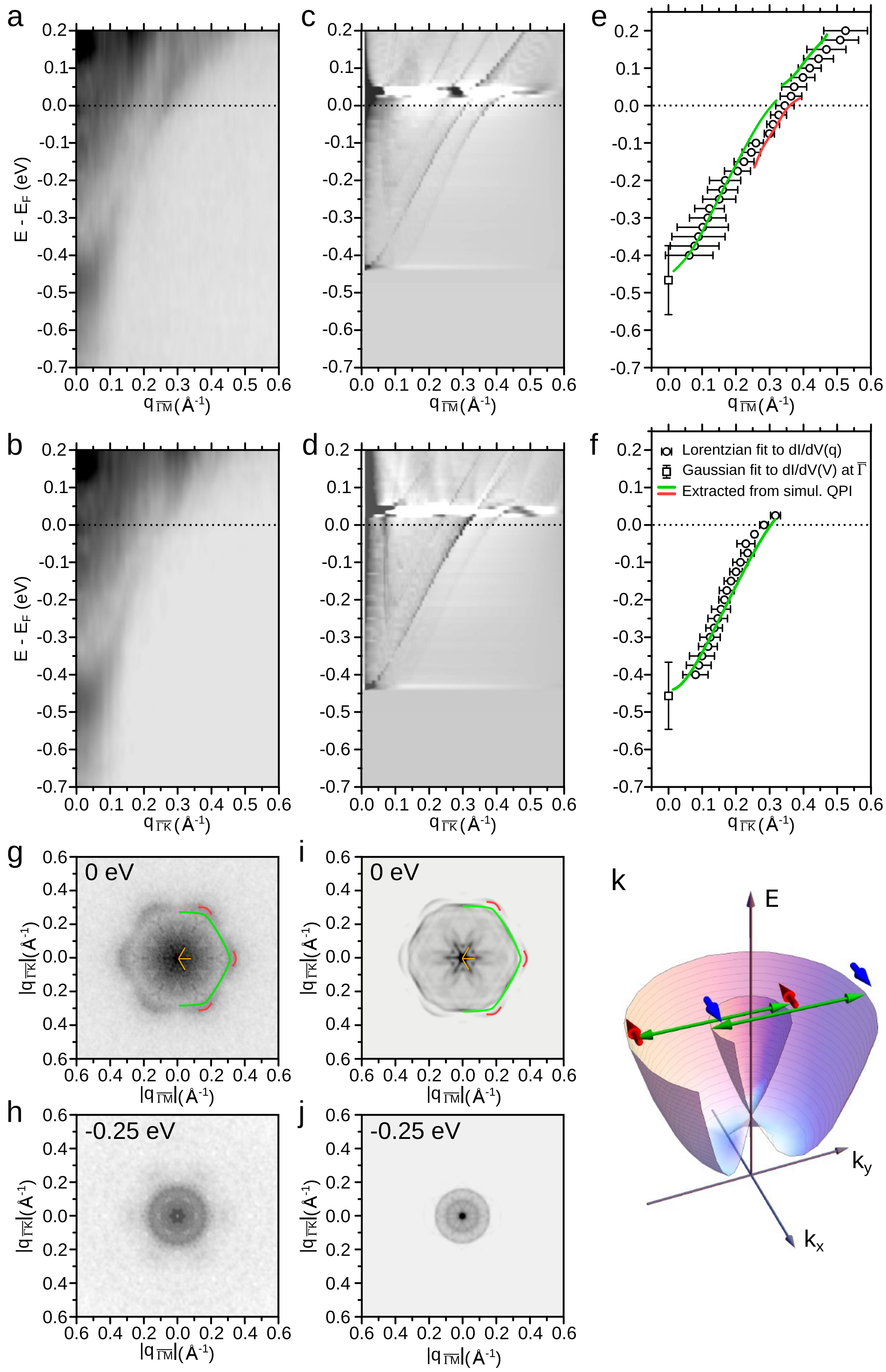

Figure 3. Spin-dependence of quasiparticle scattering in the Rashba-split surface band. (a and b) $E(\vec{q})$ plots along the $\overline{\Gamma M}$ and $\overline{\Gamma K}$ directions and (c and d) the corresponding simulated $E(\vec{q})$ plots. Peaks in dI/d$V(E, \vec{q})$ along $\overline{\Gamma M}$ and $\overline{\Gamma K}$ are obtained using Lorentzian fitting and plotted for comparison with the $E(\vec{q})$ curve extracted from (c) and (d). (e and f) Comparisons between the measured and simulated $E(\vec{q})$ relations are plotted in (e) and (f). Selected examples of measured constant energy dI/d$V(\vec{q})$ images are shown in (g) and (h), and the corresponding simulated images shown for comparison in (i) and (j). For $E - E_F = 0$ eV, the dI/d$V(E, \vec{q})$ features associated with intercontour backscattering are marked in green, and the additional features attributed to CEC warping are marked in red. (k) Illustration of intercontour backscattering, conserving spin, to which the dominant scattering events near the CBM are attributed.

measured using spin-resolved ARPES. We instead calculate the CEC using DFT as described above.

A side-by-side comparison of these dI/d$V(E, \vec{q})$ and SSP$(E, \vec{q})$ plots is shown in Figure 3. Figure 3a and b show measured dI/d$V(E, \vec{q})$ along the $\overline{\Gamma M}$ and $\overline{\Gamma K}$ directions, each showing a single prominent QPI branch extending from the conduction band minimum (CBM, here measured to be located at −0.43 eV), which we attribute to scattering of the surface state. A wedge-shaped continuum of low-wavevector QPI extends upward from around −0.2 eV. This could be caused by

DOI: 10.1021/acsnano.6b04109
ACS Nano 2016, 10, 9361−9369

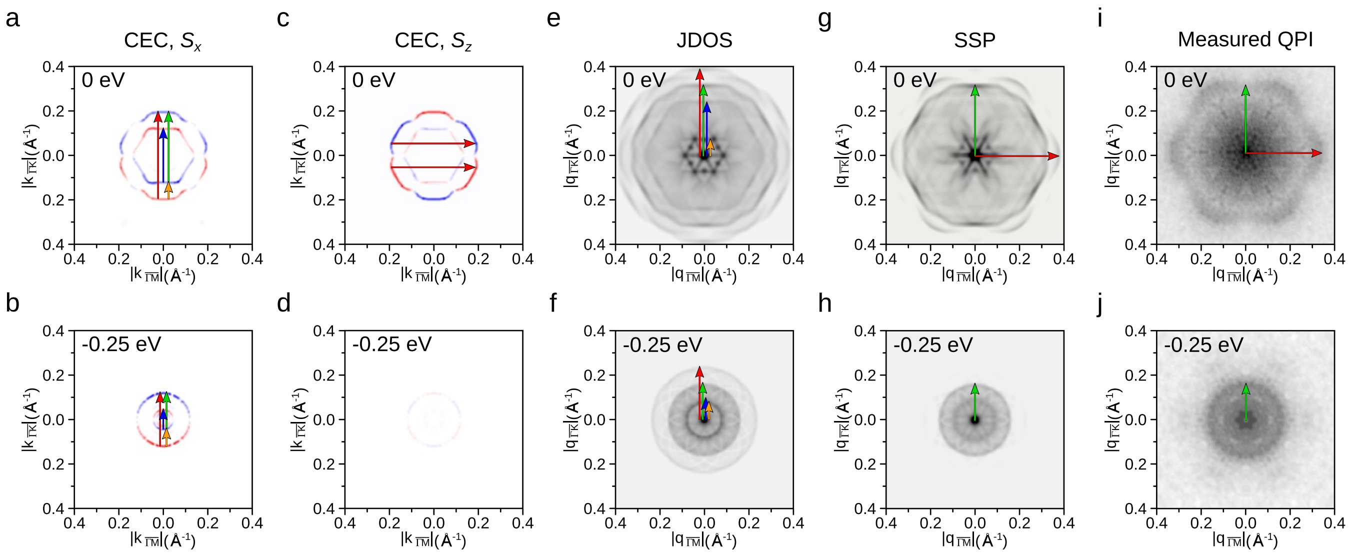

Figure 4. Scattering channels suppressed by spin conservation and origin of *intra*band scattering due to CEC warping. (a–d) Calculated spin-resolved CECs at two chosen energies (matching the selected QPI patterns shown in Figure 3), showing the projected spin components along the $\vec{x}$ direction (here set parallel to $\overline{\Gamma M}$) and in the $\vec{z}$ direction. Colored arrows mark the various scattering channels in the CECs and their resulting features in the joint-density of states (JDOS): spin-conserving intercontour (green), non-spin-conserving intercontour (orange), and two kinds of non-spin-conserving *intra*contour scattering channels (blue and red). If scattering probability is insensitive to the spins of the initial and final states, *intra*contour scattering channels can exist, as shown in the simple quasiparticle JDOS displayed in (e) and (f). With the inclusion of spin-sensitive transition matrix elements in the scattering model, we obtain the SSPs shown in (g) and (h), in which most channels shown in the simple JDOS are suppressed and which better predict the measured QPI patterns shown in (i) and (j). In (c), strong out-of-plane spin components allow *intra*contour scattering, as marked by red arrows. The resulting QPI signature, marked with horizontal red arrows, can be seen in both the calculated SSP and measured QPI patterns.

scattering in the (surface-projected) bulk conduction band or between the bulk conduction band and the surface state. Figure 3c and d show simulated SSP$(E, \vec{q})$ cuts along the $\overline{\Gamma M}$ and $\overline{\Gamma K}$ directions, also showing a main dispersive branch along both directions.

On the basis of the Rashba model, we expect that these dominant scattering wavevectors correspond to intercontour backscattering events that conserve the quasiparticle spin. This is because other possible scattering branches involve opposite or nearly opposite spin states: scattering vectors between points on opposite sides of the same contour and on the short nonbackscattering paths between the inner and outer contours. These spin-flip scattering events should be strongly suppressed. This effect is captured in the simulated SSP$(E, \vec{q})$ plots. (The scattering branches that would appear if spin-flip scattering is allowed are shown in Figure 4.) Figure 3e and f show that measured and simulated QPI branches are largely in good agreement, indicating the suppression of spin-flip scattering in the experimentally observed QPI. A schematic of the scattering processes that dominate near the CBM, namely, intercontour backscattering events, is shown in Figure 3k.

Some features seen in both the measured QPI and the SSP deviate from those naively expected based on an isotropic Rashba-like dispersion. In the SSP$(E, \vec{q})$ plot along $\overline{\Gamma M}$, another small branch (marked in red in Figure 3e) is seen near the Fermi level. This anisotropic feature can be seen in more detail in the measured and simulated QPI patterns shown in Figure 3g and i, where the expected intercontour QPI signal is marked with a green line and the additional *intra*contour signal is marked with red. We attribute it to warping of the outer ring of the constant energy contour and a resulting out-of-plane spin component allowing intracontour scattering, which would otherwise be forbidden.[3,15] Figure 4 gives the explicit demonstration of this effect: The spin-resolved constant energy contours at E_F and at −0.2 eV are shown in Figure 4a–d (along with the resulting joint-density-of-states (JDOS), SSP, and measured QPI patterns). They show the projected spin components along the $\vec{x}$ direction (here set parallel to $\overline{\Gamma M}$) and in the $\vec{z}$ direction. At the Fermi level, where the CEC has a pronounced warping, the outer contour hosts a strong out-of-plane spin component (Figure 4c), while at −0.2 eV, only a very weak out-of-plane component exists due to the high isotropy of the CEC. The resulting intracontour scattering channels are shown as red arrows on the CEC and also in the SSP and measured QPI (Figure 4g and i).

It is possible that the relative strength of this measured intracontour scattering, unforeseen using our scattering model, may stem from relatively suppressed rate for scattering involving the inner Fermi surface (including intercontour scattering) with respect to scattering involving only the outer Fermi surface, which has recently been discussed in BiTeI.[44] Near the CBM, the measured and simulated QPI dispersion behaviors are in excellent agreement and are both nearly isotropic, as is shown in Figures 3 and 4. Overall, the results displayed in Figures 3 and 4 demonstrate the anticipated suppression of spin-flip backscattering similar to that previously observed in topological insulators.

Defect Site Dependence of Quasiparticle Scattering Strength. We now turn our attention to the fact that the QPI phenomena described above arise almost entirely around the defects labeled as type B in the discussion of Figures 1 and 2. Figure 5a shows atomically resolved images of the point defects labeled above as types A, B, and C. Defects of type A are located at Te surface lattice sites and so may naturally be identified as D_{Te}. Defects with appearances similar to those of types B and C have been observed in previous STM work on

DOI: 10.1021/acsnano.6b04109
ACS Nano 2016, 10, 9361–9369

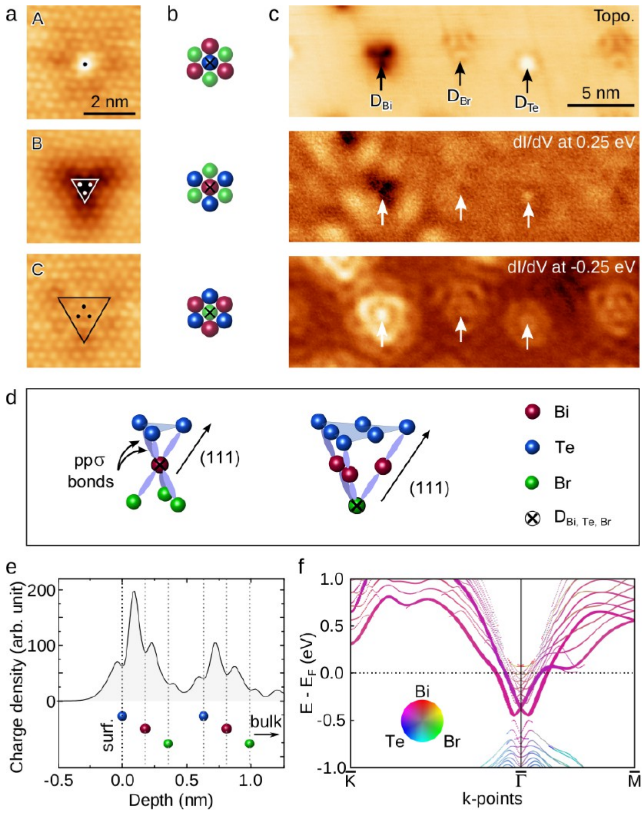

Figure 5. Defect site dependence of quasiparticle scattering strength. (a) Atomically resolved STM images of the three characteristic point defects, labeled as types A, B, and C, of the Te termination. The prominent dark lobes of type B and C defects are outlined with a white or black triangle. Te surface lattice sites around the defect pattern center are marked with white or black dots. (b) Depictions of the defect sites D_{Te}, D_{Bi}, and D_{Br} assigned to type A, B, and C defects using the *ppσ* bond model depicted in (c). (d) Topograph and corresponding d*I*/d*V* images (taken at *V* = 0.25 eV and −0.25 eV) of D_{Bi}, D_{Br}, and D_{Te} defects, showing the relative intensity of QPI electron density modulations surrounding each of them. The approximate defect locations are marked with black/white arrows in each map. While the electron density is significantly modulated around D_{Bi}, it is more uniform around D_{Te} and D_{Br}, especially at −0.25 eV, near the CBM. (e) Planar average of the electronic charge density as a function of depth along the *c*-axis. (f) Surface-projected band structure for the first three trilayers of the Te termination, with the color showing the atomic species' respective contributions.

the Te terminations of BiTeI and BiTeBr, in which they were both identified as substitutions or vacancies in the halogen atomic layer.[40,41] Here, however, we take advantage of resolution of the surface atomic lattice to note that the defect pattern centers for types B and C are located in the middle of triangles formed by Te surface lattice sites, but in triangles of different orientations. In principle one or both of these defect types could be interstitial impurities. These have been induced in similar materials by deposition and subsequent annealing of adatoms.[45] However, intrinsic interstitials have not been reported in previous work on BiTeI or BiTeBr[40,41] nor in thorough defect identifications in other similar systems.[46,47] Therefore, we suppose that type B and C defects are actually located at lattice sites in different subsurface atomic layers, either the Te layer or Br layer. But more information is needed to determine which type is located in which layer. For this we consider the *ppσ* bond chain model, which suggests that the domain of electronic influence for a given lattice site extends outward along the directions of the ⟨111⟩-oriented *ppσ* bonds until it meets the surface layer, as illustrated in Figure 5d. The spatial extent of a defect pattern at the surface is therefore proportional to the depth of the defect site.[46] In Figure 5a we show that type C has a defect pattern of greater size, so is likely located in the Br layer, while type B is located in the Bi layer (possibly a Te_{Bi} substitution).

Hence we assign defects of type A, B, and C the identities D_{Te}, D_{Bi}, and D_{Br}, respectively. However, we note that it may be possible to improve on the robustness of this identification using comparisons of measured and simulated STM defect images, as in several recent works.[45,47] The coordination environments for each are illustrated in Figure 5b. Figure 5c shows the varying intensity of electron density (measured as d*I*/d*V*) modulations surrounding different types of defect, representing differing quasiparticle scattering strengths. As mentioned above, stronger modulations appear around D_{Bi} than around either D_{Te} or D_{Br}, especially near the CBM. In order to explain this effect, we examine the calculated momentum-, depth-, and element-resolved local density of states (LDOS), which we may write as $\rho_S(z, k_x, k_y, E)$ where S denotes the atomic species and $\rho_{Total} = \sum_S \rho_S$. Figure 5e shows the momentum- and element-integrated LDOS (proportional to the planar average of electron charge density), plotted as a function of depth. A higher planar charge density is found around the z position of the Bi layer than around those of the Te and Br layers. An alternative view of the LDOS, showing $\rho_S(k_{\overline{\Gamma M}}, k_{\overline{\Gamma K}}, E)$ localized in the surface trilayers is shown in Figure 5f. The contributions to the LDOS of each atomic species are represented on an RGB color scale. The magenta color of the surface state in which we observe QPI indicates that it is dominated by orbitals from Bi (with some small contribution from Te). This is because the surface band is split off, by the strong surface polarization, from the bulk conduction band, which is derived from three Bi 6p levels (whereas the bulk valence band is derived from six bands of Te 5p and Br 4p levels).[3] The relatively strong scattering caused by D_{Bi} can therefore be attributed to the fact that defects (scattering potentials) located on the Bi sublattice of the crystal couple most strongly with the Te termination surface state due to its Bi 6p-like orbital character. (A demonstration of the same effect at the Te-terminated surface of BiTeI can be seen in Figure S1 in the Supporting Information.)

CONCLUSIONS

XPS and large-scale STM measurements reveal that our BiTeBr crystals have millimeter-scale uniform surface terminations and are probably single-domain crystals. This represents a distinct advantage over BiTeI, which features a domain-like microstructure of regions with opposite stacking orders,[8,34,39,40] meaning that crystals of macroscopic scale have no net helical spin texture. Our BiTeBr crystals on the other hand are expected to have a consistent helicity of the spin texture over macroscopic length scales, offering a more ideal platform for proof-of-concept devices exploiting strongly Rashba-split carriers to realize a variety of spintronic functions.

Although the Br-terminated surface appears to have unstable contaminations that make scanning difficult, the Te-terminated surface is highly stable with isolated C_{3v} symmetry point defects, providing scattering centers for QPI observations. Below around −0.2 eV the only measurable QPI corresponds

DOI: 10.1021/acsnano.6b04109
ACS Nano 2016, 10, 9361−9369

to scattering in the Rashba-split 2DEG-like surface band and is highly isotropic. The QPI observed near E_F does not show such ideal behavior, with anisotropy caused by band warping, and a significant low-wavevector background QPI signal, which might result from the onset of the (surface-projected) bulk conduction band. As the most ideal behavior (*i.e.*, most like the Rashba model) is found below E_F, with a view to device application, there may be a need either for electrostatic gating or to find suitable p-type surface dopants in order to move E_F down by around 0.2 eV to access carriers with the most ideal behavior.

Finally, having identified the three characteristic point defects appearing at the Te-terminated surface of BiTeBr, we explain their relative quasiparticle scattering strengths in terms of the orbital character of the band in question: Defects on the Bi sublattice strongly scatter the Te termination's surface state due to the Bi 6p-like character it inherits from the bulk conduction band, whereas defects on the Te and Br sublattices cause almost no scattering of this band through a wide energy range. This demonstration of the interplay between defect chemistry and in-plane conductance should be generalizable to a wide range of existing and emergent materials. This insight can be used in future STM experiments to help to identify unknown defects based on known orbital characteristics of quasiparticle bands or as a diagnostic tool to identify impediments to ballistic transport. It can also be used to identify the crystal lattice site where substitution impurities should be expected to couple most efficiently with carriers if so desired, for example in the case of substitutional transitional metal impurities such as in $Bi_{1-y}M_yTeX$.

In summary, we highlight BiTeBr as among the most promising systems for the exploitation of 2-D Rashba-split carriers for the realization of electric control of spin currents and examine two mechanisms governing the scattering of those carriers from point defects: (1) We confirm the suppression of spin flip scattering in the Rashba-split surface band, while noting that, near E_F, band warping gives rise to significant out-of-plane canting of spins and *intra*contour scattering channels in addition to the intercontour backscattering naively expected for the simple Rashba model. (2) We identify point defects in each atomic layer, which neatly allow us to demonstrate that various defects' scattering strengths depend on the orbital character of the surface band in which scattering occurs. This effect in particular may give generalizable insights for STM investigations of carrier behavior and defect chemistry, but also for crystal design and engineering, in a wide range of existing and emergent systems.

METHODS

Crystal Growth. BiTeBr crystals were grown using chemical vapor transport, from elements Bi and Te (of 5N purity) and from $BiBr_3$ and $TeBr_4$. An ampule was charged with the starting materials in a stoichiometric ratio. The evacuated ampule was inserted into a furnace with a temperature gradient of 450 to 480 °C, with the starting material in the hot zone. After 100 h, crystals of dimensions 5 × 8 mm^2 and thicknesses of several hundred micronmeters had grown in the cold zone of the ampule.

XPS Measurements. XPS measurements were performed using a scanning photoemission microscope (SPEM) at beamline 09A1 of the Taiwan Light Source, NSRRC,[48,49] on BiTeBr crystals that were cleaved under a pressure of around 1×10^{-10} mbar before transfer to the SPEM measurement stage. Measurements were performed at room temperature. The photon energy used was 126 eV, giving a short photoelectron escape depth for high surface sensitivity. The X-ray beam width, used without zone-plate focusing, was ~200 μm.

STM and Spectroscopic Imaging Measurements. All STM measurements were performed on BiTeBr crystals cleaved at room temperature in a preparation chamber with a base pressure lower than 1×10^{-10} mbar, before transfer to the STM chamber with a base pressure lower than 5×10^{-11} mbar. STM measurements were performed at a temperature of 4.5 K in an Omicron low-temperature STM using a chemically etched tungsten tip. For observations of QPI phenomena, the spectroscopic imaging technique was used: $dI/dV(V)$ curves were acquired using the lock-in technique (with a bias modulation of amplitude 10 mV), on each point of a spatial grid, forming a data set of $dI/dV(x, y, V)$ from which spatial $dI/dV(x, y)$ images could be extracted at each energy. Symmetrization of 2-D FFT images was performed according to the C_{3v} point group symmetry of the BiTeBr surface lattice, and examples of QPI data pre- and postsymmetrization are included in Figure S2 of the Supporting Information. STM images were processed using the WSxM software package.[50]

DFT Calculations. First-principles calculations for the projected band structure of the Te-terminated surface were performed in accordance with DFT using the PAW-LDA exchange−correlation functional as implemented in the VASP package.[51] Relativistic effects including spin−orbit coupling were accounted for. Surface-projected band structure calculations were based on a eight-trilayer slab model with a terminating layer of H atoms on the Br side and a vacuum layer of 1.88 nm. The simulated SSP plots are computed from the calculated CEC plots. The SSP is proportional to the scattering rate, determined by the relation

$$\mathrm{SSP}(\vec{q}) \propto W(\vec{q}) = \int \rho(\vec{k})\, T(\vec{q}, \vec{k})\, \rho(\vec{k} + \vec{q})\, d^2\vec{k}$$

where $T(\vec{q}, \vec{k}) = |\langle \vec{s}(\vec{k}) | \vec{s}(\vec{k} + \vec{q}) \rangle|^2$, and $\rho(\vec{k})$ can be represented by the intensity of the calculated spin-resolved CECs. $\vec{s}(\vec{k})$ are represented using the three calculated spin components for a given $\vec{k}$.

ASSOCIATED CONTENT

Supporting Information

The Supporting Information is available free of charge on the ACS Publications website at DOI: 10.1021/acsnano.6b04109.

A more detailed discussion of the XPS curves, an estimation of the Fermi velocities on the Te surface Fermi contour, an example of defect-dependent scattering strength at the Te surface of BiTeI, and an example of the effects of symmetrization on QPI data (PDF)

AUTHOR INFORMATION

Corresponding Author

*E-mail (M.-T. Lin): mtlin@phys.ntu.edu.tw.

Author Contributions

C.J.B. performed XPS measurements with assistance from SPEM instrument scientist L.Y.C. and endstation spokesperson C.H.C. C.J.B. also performed all STM measurements, data processing, and analysis, with help from C.I.L., Y.N.L., and P.Y.Y. BiTeBr crystals were grown and characterized by R.S. in the group of F.C.C. All DFT calculations were performed by P.Y.Y., under the supervision of C.M.W. C.J.B. interpreted the data and prepared the figures and manuscript with input from all authors. The project was led by M.T.L.

Notes

The authors declare no competing financial interest.

ACKNOWLEDGMENTS

This work was supported in part by the National Science Council of Taiwan through the following grants: MOST 104-2119-M-002-029 and NSC 101-2119-M-002-007.

REFERENCES

(1) Koroteev, Y. M.; Bihlmayer, G.; Gayone, J. E.; Chulkov, E. V.; Blügel, S.; Echenique, P. M.; Hofmann, P. Strong Spin-Orbit Splitting on Bi Surfaces. *Phys. Rev. Lett.* **2004**, *93*, 046403.

(2) Ast, C. R.; Henk, J.; Ernst, A.; Moreschini, L.; Falub, M. C.; Pacilé, D.; Bruno, P.; Kern, K.; Grioni, M. Giant Spin Splitting through Surface Alloying. *Phys. Rev. Lett.* **2007**, *98*, 186807.

(3) Ishizaka, K.; Bahramy, M. S.; Murakawa, H.; Sakano, M.; Shimojima, T.; Sonobe, T.; Koizumi, K.; Shin, S.; Miyahara, H.; Kimura, A.; Miyamoto, K.; Okuda, T.; Namatame, H.; Taniguchi, M.; Arita, R.; Nagaosa, N.; Kobayashi, K.; Murakami, Y.; Kumai, R.; Kaneko, Y.; et al. Giant Rashba-Type Spin Splitting in Bulk BiTeI. *Nat. Mater.* **2011**, *10*, 521−526.

(4) Lee, J. S.; Schober, G. A. H.; Bahramy, M. S.; Murakawa, H.; Onose, Y.; Arita, R.; Nagaosa, N.; Tokura, Y. Optical Response of Relativistic Electrons in the Polar BiTeI Semiconductor. *Phys. Rev. Lett.* **2011**, *107*, 117401.

(5) Wang, C.-R.; Tung, J.-C.; Sankar, R.; Hsieh, C.-T.; Chien, Y. Y.; Guo, G.-Y.; Chou, F.-C.; Lee, W.-L. Magnetotransport in Copper-Doped Noncentrosymmetric BiTeI. *Phys. Rev. B: Condens. Matter Mater. Phys.* **2013**, *88*, 081104.

(6) Ogawa, N.; Bahramy, M. S.; Murakawa, H.; Kaneko, Y.; Tokura, Y. Magnetophotocurrent in BiTeI with Rashba Spin-Split Bands. *Phys. Rev. B: Condens. Matter Mater. Phys.* **2013**, *88*, 035130.

(7) Crepaldi, A.; Moreschini, L.; Autès, G.; Tournier-Colletta, C.; Moser, S.; Virk, N.; Berger, H.; Bugnon, P.; Chang, Y. J.; Kern, K.; Bostwick, A.; Rotenberg, E.; Yazyev, O. V.; Grioni, M. Giant Ambipolar Rashba Effect in the Semiconductor BiTeI. *Phys. Rev. Lett.* **2012**, *109*, 096803.

(8) Butler, C. J.; Yang, H.-H.; Hong, J.-Y.; Hsu, S.-H.; Sankar, R.; Lu, C.-I.; Lu, H.-Y.; Ou Yang, K.-H.; Shiu, H.-W.; Chen, C.-H.; Kaun, C.-C.; Shu, G.-J.; Chou, F.-C.; Lin, M.-T. Mapping Polarization Induced Surface Band Bending on the Rashba Semiconductor BiTeI. *Nat. Commun.* **2014**, *5*, 4066.

(9) Ando, T.; Fowler, A. B.; Stern, F. Electronic Properties of Two-Dimensional Systems. *Rev. Mod. Phys.* **1982**, *54*, 437−672.

(10) Manchon, A.; Koo, H. C.; Nitta, J.; Frolov, S. M.; Duine, R. A. New Perspectives for Rashba Spin-Orbit Coupling. *Nat. Mater.* **2015**, *14*, 4360.

(11) Sinova, J.; Culcer, D.; Niu, Q.; Sinitsyn, N. A.; Jungwirth, T.; MacDonald, A. H. Universal Intrinsic Spin Hall Effect. *Phys. Rev. Lett.* **2004**, *92*, 126603.

(12) Datta, S.; Das, B. Electronic Analog of the Electro-Optic Modulator. *Appl. Phys. Lett.* **1990**, *56*, 665−667.

(13) Koga, T.; Nitta, J.; Takayanagi, H.; Datta, S. Spin-Filter Device Based on the Rashba Effect Using a Nonmagnetic Resonant Tunneling Diode. *Phys. Rev. Lett.* **2002**, *88*, 126601.

(14) Ohe, J.; Yamamoto, M.; Ohtsuki, T.; Nitta, J. Mesoscopic Stern-Gerlach Spin Filter by Nonuniform Spin-Orbit Interaction. *Phys. Rev. B: Condens. Matter Mater. Phys.* **2005**, *72*, 041308.

(15) Bahramy, M. S.; Yang, B.-J.; Arita, R.; Nagaosa, N. Emergence of Non-Centrosymmetric Topological Insulating Phase in BiTeI Under Pressure. *Nat. Commun.* **2012**, *3*, 679.

(16) Chen, Y. L.; Kanou, M.; Liu, Z. K.; Zhang, H. J.; Sobota, J. A.; Leuenberger, D.; Mo, S. K.; Zhou, B.; Yang, S.-L.; Kirchmann, P. S.; Lu, D. H.; Moore, R. G.; Hussain, Z.; Shen, Z. X.; Qi, X. L.; Sasagawa, T. Discovery of a Single Topological Dirac Fermion in the Strong Inversion Asymmetric Compound BiTeCl. *Nat. Phys.* **2013**, *9*, 704−708.

(17) Ohmura, A.; Higuchi, Y.; Ochiai, T.; Kanou, M.; Ishikawa, F.; Nakano, S.; Nakayama, A.; Yamada, Y.; Sasagawa, T. Pressure-Induced Topological Phase Transition in Polar-Semiconductor BiTeBr. 2016, *arXiv:1609.02274*.

(18) Kulbachinskii, V. A.; Kytin, V. G.; Kudryashov, A. A.; Kuznetsov, A. N.; Shevelkov, A. V. On the Electronic Structure and Thermoelectric Properties of BiTeBr and BiTeI Single Crystals and of BiTeI with the Addition of BiI_3 and CuI. *J. Solid State Chem.* **2012**, *193*, 154−160.

(19) Shevelkov, A. V.; Dikarev, E. V.; Shpanchenko, R. V.; Popovkin, B. A. Crystal Structures of Bismuth Tellurohalides BiTeX (X = Cl, Br, I) from X-ray Powder Diffraction Data. *J. Solid State Chem.* **1995**, *114*, 379−384.

(20) Eremeev, S. V.; Rusinov, I. P.; Nechaev, I. A.; Chulkov, E. V. Rashba Split Surface States in BiTeBr. *New J. Phys.* **2013**, *15*, 075015.

(21) Sakano, M.; Bahramy, M. S.; Katayama, A.; Shimojima, T.; Murakawa, H.; Kaneko, Y.; Malaeb, W.; Shin, S.; Ono, K.; Kumigashira, H.; Arita, R.; Nagaosa, N.; Hwang, H. Y.; Tokura, Y.; Ishizaka, K. Strongly Spin-Orbit Coupled Two-Dimensional Electron Gas Emerging Near the Surface of Polar Semiconductors. *Phys. Rev. Lett.* **2013**, *110*, 107204.

(22) Landolt, G.; Eremeev, S. V.; Tereshchenko, O. E.; Muff, S.; Slomski, B.; Kokh, K. A.; Kobayashi, M.; Schmitt, T.; Strocov, V. N.; Osterwalder, J.; Chulkov, E. V.; Hugo Dil, J. Bulk and Surface Rashba Splitting in Single Termination BiTeCl. *New J. Phys.* **2013**, *15*, 085022.

(23) Moreschini, L.; Autès, G.; Crepaldi, A.; Moser, S.; Johannsen, J. C.; Kim, K. S.; Berger, H.; Bugnon, P.; Magrez, A.; Denlinger, J.; Rotenberg, E.; Bostwick, A.; Yazyev, O. V.; Grioni, M. Bulk and Surface Band Structure of the New Family of Semiconductors BiTeX (X = I, Br, Cl). *J. Electron Spectrosc. Relat. Phenom.* **2015**, *201*, 115−120.

(24) Pascual, J. I.; Bihlmayer, G.; Koroteev, Y. M.; Rust, H.-P.; Ceballos, G.; Hansmann, M.; Horn, K.; Chulkov, E. V.; Blügel, S.; Echenique, P. M.; Hofmann, P. Role of Spin in Quasiparticle Interference. *Phys. Rev. Lett.* **2004**, *93*, 196802.

(25) El-Kareh, L.; Sessi, P.; Bathon, T.; Bode, M. Quantum Interference Mapping of Rashba-Split Bloch States in Bi/Ag(111). *Phys. Rev. Lett.* **2013**, *110*, 176803.

(26) Steinbrecher, M.; Harutyunyan, H.; Ast, C. R.; Wegner, D. Rashba-Type Spin Splitting from Interband Scattering in Quasiparticle Interference Maps. *Phys. Rev. B: Condens. Matter Mater. Phys.* **2013**, *87*, 245436.

(27) Hoffman, J. E.; McElroy, K.; Lee, D.-H.; Lang, K. M.; Eisaki, H.; Uchida, S.; Davis, J. C. Imaging Quasiparticle Interference in $Bi_2Sr_2CaCu_2O_{8+\delta}$. *Science* **2002**, *297*, 1148−1151.

(28) Aynajian, P.; da Silva Neto, E. H.; Gyenis, A.; Baumbach, R. E.; Thompson, J. D.; Fisk, Z.; Bauer, E. D.; Yazdani, A. Visualizing Heavy Fermions Emerging in a Quantum Critical Kondo Lattice. *Nature* **2012**, *486*, 201−206.

(29) Roushan, P.; Seo, J.; Parker, C. V.; Hor, Y. S.; Hsieh, D.; Qian, D.; Richardella, A.; Hasan, M. Z.; Cava, R. J.; Yazdani, A. Topological Surface States Protected from Backscattering by Chiral Spin Texture. *Nature* **2009**, *460*, 1106−1109.

(30) Zhang, T.; Cheng, P.; Chen, X.; Jia, J.-F.; Ma, X.; He, K.; Wang, L.; Zhang, H.; Dai, X.; Fang, Z.; Xie, X.; Xue, Q.-K. Experimental Demonstration of Topological Surface States Protected by Time-Reversal Symmetry. *Phys. Rev. Lett.* **2009**, *103*, 266803.

(31) Alpichshev, Z.; Analytis, J. G.; Chu, J. H.; Fisher, I. R.; Chen, Y. L.; Shen, Z. X.; Fang, A.; Kapitulnik, A. STM Imaging of Electronic Waves on the Surface of Bi_2Te_3: Topologically Protected Surface States and Hexagonal Warping Effects. *Phys. Rev. Lett.* **2010**, *104*, 016401.

(32) Jeon, S.; Zhou, B. B.; Gyenis, A.; Feldman, B. E.; Kimchi, I.; Potter, A. C.; Gibson, Q. D.; Cava, R. J.; Vishwanath, A.; Yazdani, A. Landau Quantization and Quasiparticle Interference in the Three-Dimensional Dirac Semimetal Cd_3As_2. *Nat. Mater.* **2014**, *13*, 851−856.

(33) Zheng, H.; Xu, S.-Y.; Bian, G.; Guo, C.; Chang, G.; Sanchez, D. S.; Belopolski, I.; Lee, C.-C.; Huang, S. M.; Zhang, X.; Sankar, R.; Alidoust, N.; Chang, T.-R.; Wu, F.; Neupert, T.; Chou, F.-C.; Jeng, H.-T.; Yao, N.; Bansil, A.; Jia, S.; et al. Atomic-Scale Visualization of Quantum Interference on a Weyl Semimetal Surface by Scanning Tunneling Microscopy. *ACS Nano* **2016**, *10*, 1378−1385.

DOI: 10.1021/acsnano.6b04109
ACS Nano 2016, 10, 9361−9369

(34) Kohsaka, Y.; Kanou, M.; Takagi, H.; Hanaguri, T.; Sasagawa, T. Imaging Ambipolar Two-Dimensional Carriers Induced By The Spontaneous Electric Polarization of a Polar Semiconductor BiTeI. *Phys. Rev. B: Condens. Matter Mater. Phys.* **2015**, *91*, 245312.
(35) Tinkham, M. *Introduction to Superconductivity*; McGraw-Hill: New York, 1996; pp 79−81.
(36) Derry, P. G.; Mitchell, A. K.; Logan, D. E. Quasiparticle Interference from Magnetic Impurities. *Phys. Rev. B: Condens. Matter Mater. Phys.* **2015**, *92*, 035126.
(37) Stróżecka, A.; Eiguren, A.; Pascual, J. Quasiparticle Interference Around a Magnetic Impurity on a Surface with Strong Spin-Orbit Coupling. *Phys. Rev. Lett.* **2011**, *107*, 186805.
(38) Yoshizawa, S.; Nakamura, F.; Taskin, A. A.; Iimori, T.; Nakatsuji, K.; Matsuda, I.; Ando, Y.; Komori, F. Scanning Tunneling Spectroscopy Study of Quasiparticle Interference on the Dual Topological Insulator $Bi_{1-x}Sb_x$. *Phys. Rev. B: Condens. Matter Mater. Phys.* **2015**, *91*, 045423.
(39) Sankar, R.; Panneer Muthuselvam, I.; Butler, C. J.; Liou, S.-C.; Chen, B.-H.; Chu, M.-W.; Lee, W.-L.; Lin, M.-T.; Jayavel, R.; Chou, F.-C. Room Temperature Agglomeration for the Growth of BiTeI Single Crystals With a Giant Rashba Effect. *CrystEngComm* **2014**, *16*, 8678.
(40) Fiedler, S.; El-Kareh, L.; Eremeev, S. V.; Tereshchenko, O. E.; Seibel, C.; Lutz, P.; Kokh, K. A.; Chulkov, E. V.; Kuznetsova, T. V.; Grebennikov, V. I.; Bentmann, H.; Bode, M.; Reinert, F. Defect and Structural Imperfection Effects on the Electronic Properties of BiTeI Surfaces. *New J. Phys.* **2014**, *16*, 075013.
(41) Fiedler, S.; Bathon, T.; Eremeev, S. V.; Tereshchenko, O. E.; Kokh, K. A.; Chulkov, E. V.; Sessi, P.; Bentmann, H.; Bode, M.; Reinert, F. Termination-Dependent Surface Properties in the Giant-Rashba Semiconductors BiTeX (X = Cl, Br, I). *Phys. Rev. B: Condens. Matter Mater. Phys.* **2015**, *92*, 235430.
(42) Tournier-Colletta, C.; Autès, G.; Kierren, B.; Bugnon, P.; Berger, H.; Fagot-Revurat, Y.; Yazyev, O. V.; Grioni, M.; Malterre, D. Atomic and Electronic Structure of a Rashba p-n Junction at the BiTeI Surface. *Phys. Rev. B: Condens. Matter Mater. Phys.* **2014**, *89*, 085402.
(43) Ast, C. R.; Wittich, G.; Wahl, P.; Vogelgesang, R.; Pacilé, D.; Falub, M. C.; Moreschini, L.; Papagno, M.; Grioni, M.; Kern, K. Local Detection of Spin-Orbit Splitting by Scanning Tunneling Spectroscopy. *Phys. Rev. B: Condens. Matter Mater. Phys.* **2007**, *75*, 201401.
(44) Sasaki, M.; Kim, K. M.; Ohnishi, A.; Kitaura, M.; Tomita, N.; Kulbachinskii, V. A.; Kim, K. S.; Kim, H. J. Interplay Between Disorder and Inversion Symmetry: Extreme Enhancement of the Mobility Near the Weyl Point in BiTeI. *Phys. Rev. B: Condens. Matter Mater. Phys.* **2015**, *92*, 205121.
(45) West, D.; Sun, Y. Y.; Zhang, S. B. Identification of Magnetic Dopants on the Surfaces of Topological Insulators: Experiment and Theory for Fe on Bi_2Te_3(111). *Phys. Rev. B: Condens. Matter Mater. Phys.* **2012**, *85*, 081305.
(46) Jiang, Y.; Sun, Y. Y.; Chen, M.; Wang, Y.; Li, Z.; Song, C.; He, K.; Wang, L.; Chen, X.; Xue, Q.-K.; Ma, X.; Zhang, S. B. Fermi-Level Tuning of Epitaxial Sb_2Te_3 Thin Films on Graphene by Regulating Intrinsic Defects and Substrate Transfer Doping. *Phys. Rev. Lett.* **2012**, *108*, 066809.
(47) Bathon, T.; Achilli, S.; Sessi, P.; Golyashov, V. A.; Kokh, K. A.; Tereschenko, O. E.; Bode, M. Experimental Realization of a Topological p-n Junction by Intrinsic Defect Grading. *Adv. Mater. (Weinheim, Ger.)* **2016**, *28*, 2183−2188.
(48) Hong, I. H.; Lee, T. H.; Yin, G. C.; Wei, D. H.; Juang, J. M.; Dann, T. E.; Klauser, R.; Chuang, T. J.; Chen, C. T.; Tsang, K. L. Performance of the SRRC Scanning Photoelectron Microscope. *Nucl. Instrum. Methods Phys. Res., Sect. A* **2001**, *467*, 905−908.
(49) Klauser, R.; Hong, I.-H.; Lee, T.-H.; Yin, G.-C.; Wei, D.-H.; Tsang, K.-L.; Chuang, T.-J.; Wang, S.-C.; S, G.; Zharnikov, M.; Liao, J.-D. Zone-Plate-Based Scanning Photoelectron Microscopy at SRRC: Performance and Applications. *Surf. Rev. Lett.* **2002**, *9*, 213−222.
(50) Horcas, I.; Fernández, R.; Gómez-Rodríguez, J. M.; Colchero, J.; Gómez-Herrero, J.; Baro, A. M. WSXM: A Software for Scanning Probe Microscopy and a Tool for Nanotechnology. *Rev. Sci. Instrum.* **2007**, *78*, 013705.
(51) Kresse, G. From Ultrasoft Pseudopotentials to the Projector Augmented-Wave Method. *Phys. Rev. B: Condens. Matter Mater. Phys.* **1999**, *59*, 1758−1775.

DOI: 10.1021/acsnano.6b04109
ACS Nano 2016, 10, 9361−9369